



A Journal of the Gesellschaft Deutscher Chemiker

Angewandte Chemie

GDCh

International Edition

www.angewandte.org

Accepted Article

Title: Fabricating Dual-Atom Iron Catalysts for Efficient Oxygen Evolution Reaction: A Heteroatom Modulator Approach

Authors: Yong-Sheng Wei, Liming Sun, Miao Wang, Jinhua Hong, Lianli Zou, Hongwen Liu, Yu Wang, Mei Zhang, Zheng Liu, Yinwei Li, Satoshi Horike, Kazu Suenaga, and Qiang Xu

This manuscript has been accepted after peer review and appears as an Accepted Article online prior to editing, proofing, and formal publication of the final Version of Record (VoR). This work is currently citable by using the Digital Object Identifier (DOI) given below. The VoR will be published online in Early View as soon as possible and may be different to this Accepted Article as a result of editing. Readers should obtain the VoR from the journal website shown below when it is published to ensure accuracy of information. The authors are responsible for the content of this Accepted Article.

To be cited as: *Angew. Chem. Int. Ed.* 10.1002/anie.202007221

Link to VoR: <https://doi.org/10.1002/anie.202007221>

Fabricating Dual-Atom Iron Catalysts for Efficient Oxygen Evolution Reaction: A Heteroatom Modulator Approach

Yong-Sheng Wei,^[a] Liming Sun,^[a,b] Miao Wang,^[a] Jinhua Hong,^[c] Lianli Zou,^[a] Hongwen Liu,^[a] Yu Wang,^[a] Mei Zhang,^[a] Zheng Liu,^[d] Yinwei Li,^[e] Satoshi Horike,^[a,f] Kazu Suenaga,^[c] Qiang Xu*^[a,g]

- [a] Dr. Y.-S. Wei, Dr. L. Sun, M. Wang, Dr. L. Zou, H. Liu, Dr. Y. Wang, Dr. M. Zhang, Prof. S. Horike, Prof. Q. Xu
AIST-Kyoto University Chemical Energy Materials Open Innovation Laboratory (ChEM-OIL), National Institute of Advanced Industrial Science and Technology (AIST), Sakyo-ku, Kyoto 606-8501, Japan.
E-mail: q.xu@aist.go.jp
- [b] Dr. L. Sun
Jiangsu Key Laboratory of Green Synthetic Chemistry for Functional Materials, Department of Chemistry, School of Chemistry and Materials Science, Jiangsu Normal University, Xuzhou, 221116, P. R. China.
- [c] Dr. J. Hong, Prof. K. Suenaga
Nanomaterials Research Institute, National Institute of Advanced Industrial Science and Technology (AIST), Tsukuba 305-8565, Japan.
- [d] Dr. Z. Liu
Innovative Functional Materials Research Institute, National Institute of Advanced Industrial Science and Technology (AIST), 2266-98 Anagahora, Shimoshidami, Moriyamaku, Nagoya, Aichi, 463-8560, Japan.
- [e] Prof. Y. Li
Laboratory of Quantum Materials Design and Application, School of Physics and Electronic Engineering, Jiangsu Normal University Xuzhou 221116, P. R. China.
- [f] Prof. S. Horike
Institute for Integrated Cell-Material Sciences (WPI-iCeMS), Institute for Advanced Study, Kyoto University, Sakyo-ku, Kyoto 606-8501, Japan.
- [g] Prof. Q. Xu
Research Institute of Electrochemical Energy, National Institute of Advanced Industrial Science and Technology (AIST), Ikeda, Osaka 563-8577, Japan.

Supporting information for this article is given via a link at the end of the document.

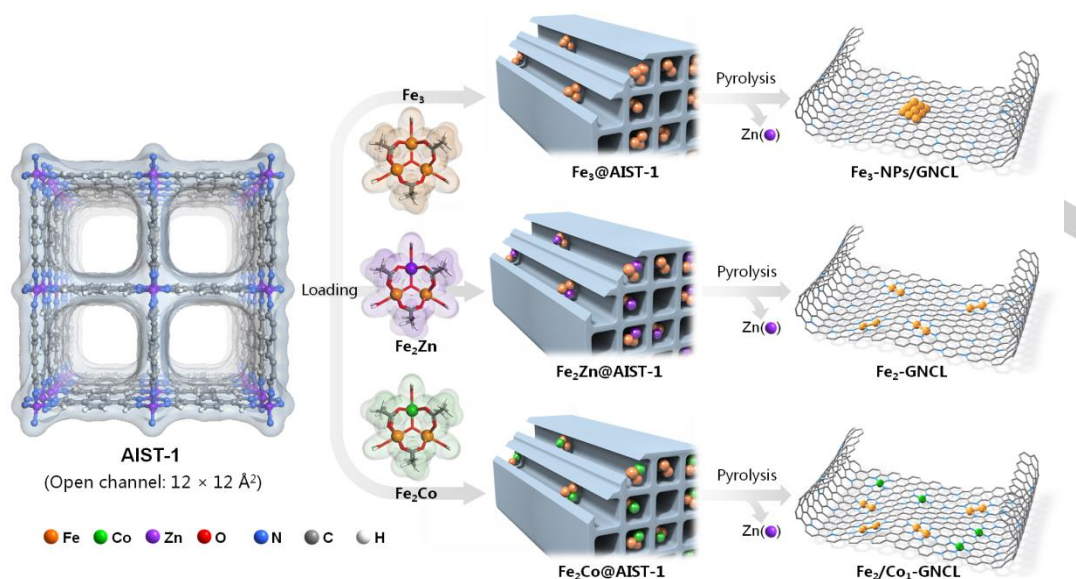
Abstract: Understanding the thermal aggregation behaviors of metal atoms is of significant importance for precise synthesis of supported metal clusters. Here, derived from a metal-organic framework encapsulating a trinuclear $\text{Fe}^{\text{III}}_2\text{Fe}^{\text{II}}$ complex (denoted as Fe_3) within the channels, a well-defined nitrogen-doped carbon layer is fabricated as an ideal support for stabilizing the generated iron nanoclusters. Atomic replacements of the Fe^{II} by other metal(II) ions (e.g., $\text{Zn}^{\text{II}}/\text{Co}^{\text{II}}$) via synthesizing isostructural trinuclear-complex precursors ($\text{Fe}_2\text{Zn}/\text{Fe}_2\text{Co}$), namely the “heteroatom modulator approach”, realizes the inhibition of iron atoms aggregating toward nanoclusters with formation of a stable iron dimer in an optimal metal-nitrogen moiety within the carbon layer, clearly identified by direct transmission electron microscope imaging with X-ray absorption fine structure analyses. Further, the supported iron dimer, serving as cooperative metal-metal sites, has been experimentally demonstrated for efficient oxygen evolution catalysis. Our findings offer an atomic insight to guide the future design of ultrasmall metal clusters bearing outstanding catalytic capabilities for the vital chemical transformations.

Introduction

Ultrasmall metal clusters (USMCs), containing merely a few metal atoms, have received considerable attention owing to their extraordinary electronic structures and catalytic behaviors compared with metal particles and even single atoms.^[1] Ligand chelation^[2] and solid-support^[3] have emerged as two efficient synthesis strategies to stabilize and characterize the USMCs.^[4] Particularly, the former can provide homogeneous metal cluster-based complexes with accurately defined structures determined by crystallographic methods, while they hardly find practical applications in catalysis owing to their inherent instability in reaction solution or even exposure to the air.^[5] In clear contrast,

USMCs supported on solids, mainly oxides (e.g., MgO ,^[6] Fe_3O_4 ,^[3a] SiO_2 ,^[3b] and TiO_2 ^[7]) are considered as the much more robust ones, but usually containing inhomogeneous metal nuclearities caused by non-ideal metal precursors or further aggregation of the generated metal clusters on supports induced by harsh synthesis conditions.^[6, 8] These synthetic uncertainties actually pose huge challenges in precise construction of supported USMCs, because their nature would be significantly changed by adding or removing only one atom from the cluster systems.^[9]

In this context, metal-organic frameworks (MOFs),^[10] constructed by metal ions/clusters and organic linkers,^[11] have been widely utilized as starting materials for thermally preparing porous carbons.^[12] By virtue of robust metal-heteroatoms (N/O/S) coordinative bonds,^[13] MOF-derived carbons are able to serve as ideal alternates to support USMCs,^[12d, 12e, 14] which can be readily employed in many catalytic applications, especially electrocatalysis owing to their excellent stability in harsh (e.g., strong acid or base) electrolytes, superior electrical conductivity, and extremely high surface areas accessible to reactants.^[12e, 15] It should be noted that direct carbonization of the target metal-based MOFs usually result in miscellaneous metal species including particles, clusters, and single atoms in a system,^[1d, 1e, 16] which actually brings serious difficulties for the identification of active metals.^[17] To address this issue, MOFs are also capable of encapsulating crystallographically determined small metal complexes within the channels, which probably produces suitable precursors for preparing supported well-defined USMCs.^[18] Nevertheless, owing to the lack of ideal platform MOFs or small metal complexes, it is still difficult to find reports of uniform metal clusters containing a specific number of metal atoms stabilized on MOF-derived carbons, let alone fully understand the clustering fashions toward certain numbers and



Scheme 1. Schematic illustration of the heteroatom modulator approach for fabricating dual-atom iron catalysts on carbon layer.

species of metal atoms, which would profoundly facilitate guiding the future design and synthesis of supported USMCs at atomic scale.

Herein, we used a unique MOF, structurally featuring abundant ordered aromatic ring arrays, which enables thermally upgrade as a nitrogen-doped carbon layer. Based on this MOF separately loading a series of trinuclear complexes: $\text{Fe}^{\text{III}}_2\text{M}^{\text{II}}(\mu_2\text{-O})(\text{CH}_3\text{COO})_6(\text{H}_2\text{O})_3$ (denoted as Fe_2M , $\text{M} = \text{Fe}, \text{Zn}, \text{Co}$) as shown in Scheme 1, we develop a “Heteroatom Modulator Approach” (HMA) for the first time, through tactfully introducing the second metal ions (Zn/Co) into the Fe-complexes, to realize an effective modulation for the aggregation states of iron atoms from nanocluster to dimer, the latter of which has been experimentally demonstrated for efficient oxygen evolution catalysis.

Results and Discussion

Single-Crystal Structural Analyses of AIST-1.

Solvothermal reactions of zinc acetate dihydrate, 1,4-di(1H-pyrazol-4-yl)benzene (H_2BPB) and HBF_4 aqueous solution in N,N -dimethylformamide (DMF) yielded colorless block micro-crystals ($> 100 \mu\text{m}$) formulated as $[\text{Zn}(\text{BPB})]\cdot\text{guest}$ (AIST-1, AIST = National Institute of Advanced Industrial Science and Technology) (Figure 1a). Single crystal X-ray diffraction (SCXRD) analysis shows that its asymmetric unit (space group $P4_322$) is composed by half of $\text{Zn}(\text{II})$ ion and half of BPB^{2-} ligand (Figures 1b, S1 and Tables S1, S2). Each $\text{Zn}(\text{II})$ center is coordinated in a tetrahedral geometry with four nitrogen (N) atoms from four independent BPB^{2-} ligands, in which two neighboring $\text{Zn}(\text{II})$ ions are bridged by two pyrazol (pz) rings, forming one-dimensional (1D) chains $[\text{Zn}(\text{pz})_2]_n$ along the c -axis.^[19] By virtue of ordered aromatic ring arrays from the BPB^{2-} spacers side-by-side (Figure 1c), the chains are further extended into a (4,4)-connected three-dimensional (3D) architecture with pts topology,^[20] featuring square edge-shared channels ($\sim 12 \times 12 \text{ \AA}^2$) (Figures 1d and S1). Remarkably, the

structural integrity and porosity of activated AIST-1 was well-maintained and confirmed by N_2 sorption experiments (77 K), which showed a type-I isotherm with a saturated uptake of $513 \text{ cm}^3 \text{ g}^{-1}$ and reasonable pore size distribution ($\sim 12 \text{ \AA}$) (Figures S2a and S2b), giving an apparent Brunauer-Emmett-Teller (BET) surface areas of $2233 \text{ m}^2 \text{ g}^{-1}$ and pore volumes of $0.943 \text{ cm}^3 \text{ g}^{-1}$, respectively (Table S3). Obviously, the unique structural characters, especially the ordered aromatic ring arrays, of AIST-1 possibly make it an ideal candidate to fabricate 2D well-defined carbons with a high degree of graphitization under controllable thermal transformation.

Preparation and Structural Characterization of GNCL.

Carbonization of AIST-1 micro-crystals at $1000 \text{ }^\circ\text{C}$ in an Ar flow resulted in the formation of a morphology-preserved bulk nitrogen-doped carbon (BNC) (Figure S3). Powder X-ray diffraction (PXRD) of the BNC shows broad peaks at 23.6° and 43.6° , corresponding to the (002) and (101) planes of graphitic carbon (Figure S2c), which is further verified by the graphene(G)-band at 1590 cm^{-1} of Raman spectra (Figure S2d). Impressively, SEM analyses demonstrate the existence of uniform carbon layer on the surface of BNC (Figures 1e, 1f and S3), which motivates us to downsize the crystals of AIST-1 precursor to attempt complete transformation to fabricate carbon layers.^[21] Accordingly, merely without HBF_4 aqueous solution, nano-crystals ($< 100 \text{ nm}$) of AIST-1 was successfully synthesized from zinc acetate dihydrate and H_2BPB in hot DMF (Figures 1g, S2a and S4), which presents similar N_2 adsorption isotherms (in low relative pressure range: $P/P_0 < 0.9$) and pore size distributions with these of micro-crystals (Figure S2b and Table S3). Nevertheless, a drastically rising adsorption isotherm at P/P_0 of 0.9-1.0 was solely observed in nano-crystals of AIST-1 indicating the presence of abundant slits caused by the stacked nano-crystals.^[22] As expected, similar pyrolysis toward the obtained nano-crystals resulted in the uniform formation of graphitized nitrogen-doped carbon layer (GNCL), as observed by TEM images (Figures 1h and S5-S7). Besides the graphitic peaks in the PXRD patterns of GNCL, the absence of additional

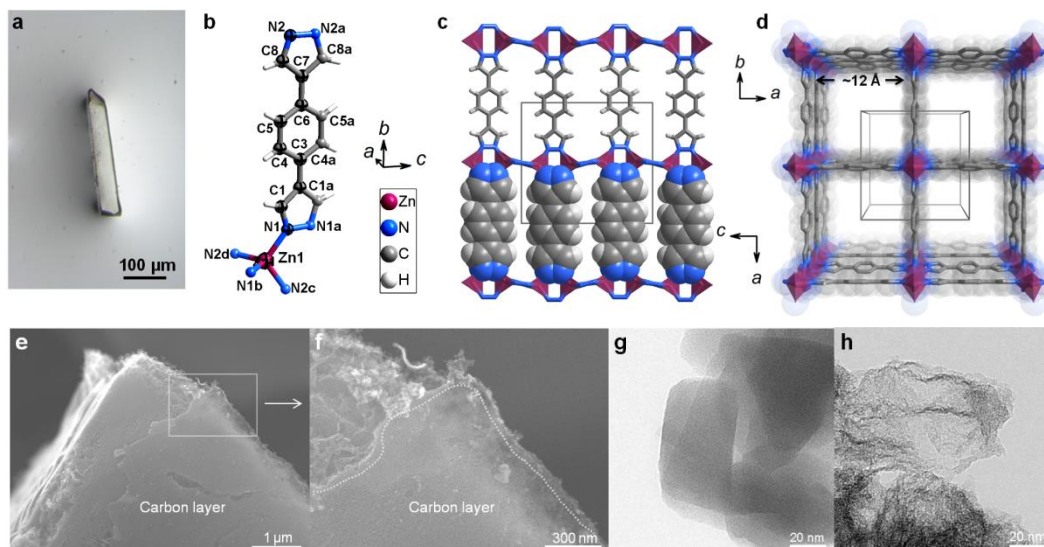


Figure 1. (a) Optical microscope image of the micro-crystals of AIST-1. (b) Perspective view of the coordination environments in AIST-1. (c) Long-range ordered aromatic ring arrays and (d) single-crystal structure along the *c*-axis of AIST-1. (e, f) SEM and enlarged image of the BNC. The white dashed circles indicate the boundary of carbon layer. (g, h) TEM images of the nano-crystals of AIST-1 and GNCL, respectively.

peaks confirms an in situ removal of the most of Zn metal (boiling point of 907 °C) at 1000 °C from the carbon matrix (Figures S2c and S8). X-ray photoelectron spectroscopy (XPS) and elemental (CHN) analyses reveal the high nitrogen (N) content (~3%) in the GNCL (Figure S8 and Table S4). To verify this MOF-topology-dependent carbonization for preparing carbon layer, SOD-[Zn(2-methylimidazole)₂] (ZIF-8) and SOD-[Zn(benzimidazole)₂] (ZIF-7),^[23] similarly constructed by Zn²⁺ and azolate ligands with AIST-1 but possessing different network topology, were employed as precursors to carry out the same thermal treatments (Figures S9 and S10). As a result, pyrolysis of both ZIF-8 and ZIF-7 nano-crystals (< 100 nm) gave morphology-retained carbon nano-particles from AIST-1, which greatly supports the above-mentioned transformation mechanism of carbon layer formation by predesigning desirable arrangement of the aromatic rings in specific topology networks.

Thermal Clustering of Metal Atoms on MOF-Derived Carbon.

Considering the highly open channels of AIST-1, our target trinuclear metal complexes can be post-synthetically immobilized into this MOF precursor to carry out the HMA strategy. First of all, the three trinuclear complexes, namely Fe^{III}₂M^{II}(μ₃-O)(CH₃COO)₆(H₂O)₃ (M = Fe, Zn, Co) (denoted as Fe₃, Fe₂Zn and Fe₂Co) were synthesized and structurally determined by series of characterizations including SCXRD, PXRD, Fourier-transform infrared spectroscopy (FT-IR), XPS, and XAFS (Figures 2a-2c, S11-S15 and Tables S2, S5). Careful structure analyses confirm that Fe₃, Fe₂Zn and Fe₂Co possess similar trinuclear structures and smaller sizes (~9.5×10×11.5 Å³) than that of the channels of AIST-1 (Figures S12a and S16). Double-solvent method (DSM)^[24] was then utilized to perform the separate encapsulations of these three trinuclear complexes into AIST-1, giving Fe₃@AIST-1, Fe₂Zn@AIST-1, and Fe₂Co@AIST-1, respectively (Figures S17-S23). For comparison, a conventionally solvothermal preparation gave Fe₁Co₁/AIST-1 by directly doping Fe(OAc)₂&Co(OAc)₂ (molar ratio = 2:1) into the starting materials during the synthesis of AIST-1 (Figure S24), which is capable of resulting in a homogeneous distribution of Fe, Co, Zn elements on the host-

framework of the Fe₁Co₁/AIST-1 unlike the specific combinations of Fe and Co atoms in Fe₂Co@AIST-1 (Figures S25 and S26).

Afterwards, pyrolysis of Fe₃@AIST-1, Fe₂Zn@AIST-1, Fe₂Co@AIST-1, and Fe₁Co₁/AIST-1 achieved the formation of Fe₃-NPs/GNCL, Fe₂-GNCL, Fe₂/Co₁-GNCL, and Fe₁/Co₁-GNCL, respectively. As expected, TEM images reveal that these obtained materials featured the similar carbon layer morphology with the bare substrate GNCL (Figures S27-S32). PXRD patterns confirm that there are no large metal particles in these samples (Figure S33), while the magnified observations exhibit several iron USMCs (1–2 nm) in the Fe₃-NPs/GNCL, as confirmed by high angle annular dark-field scanning transmission electron microscopy (HAADF-STEM) images and EDS mapping (Figures 2d and S34). In contrast, no obvious large metal clusters were observed in Fe₂-GNCL, Fe₂/Co₁-GNCL, and Fe₁/Co₁-GNCL (Figures S35-S43). To further directly elucidate these metal atoms, more powerful atomic-resolution characterizations, namely HAADF-STEM coupled with electron energy-loss (EEL) spectroscopy were carried out (Figures 2e-2i, S44, and S45). It should be noted that the well-defined carbon layer substrate of GNCL offers an ideal imaging platform to visualize structural details at the atomic level.^[17] As illustrated in the HAADF-STEM images for the Fe₂-GNCL (Figure 2e), many small bright spot pairs (highlighted in yellow boxes) are clearly observed and evenly dispersed on the carbon layer. Additionally, the well-dispersed dual sites with an approximate distance of ca. 2.6 Å can be clearly identified in the accessional intensity profiles (Figure 2f), indicating the strong interaction between the two atoms. Given the heavier Fe atom in comparison to C and N atoms, the dual spots should be dual iron atoms. Significantly, the similar pairs of spots can be also discovered in the Fe₂/Co₁-GNCL revealed by the HAADF-STEM images (Figures 2g-2i), together with many single dots (blue circles) (Figures 2g and S44). Furthermore, the single atom EEL spectroscopy^[17a] exclusively confirm that the bright dual dots correspond to the dual iron atoms, while the single dots can be recognized as Co atoms (Figures 2g and S44). In contrast, there are only individual spots in Fe₁/Co₁-GNCL separated by at least

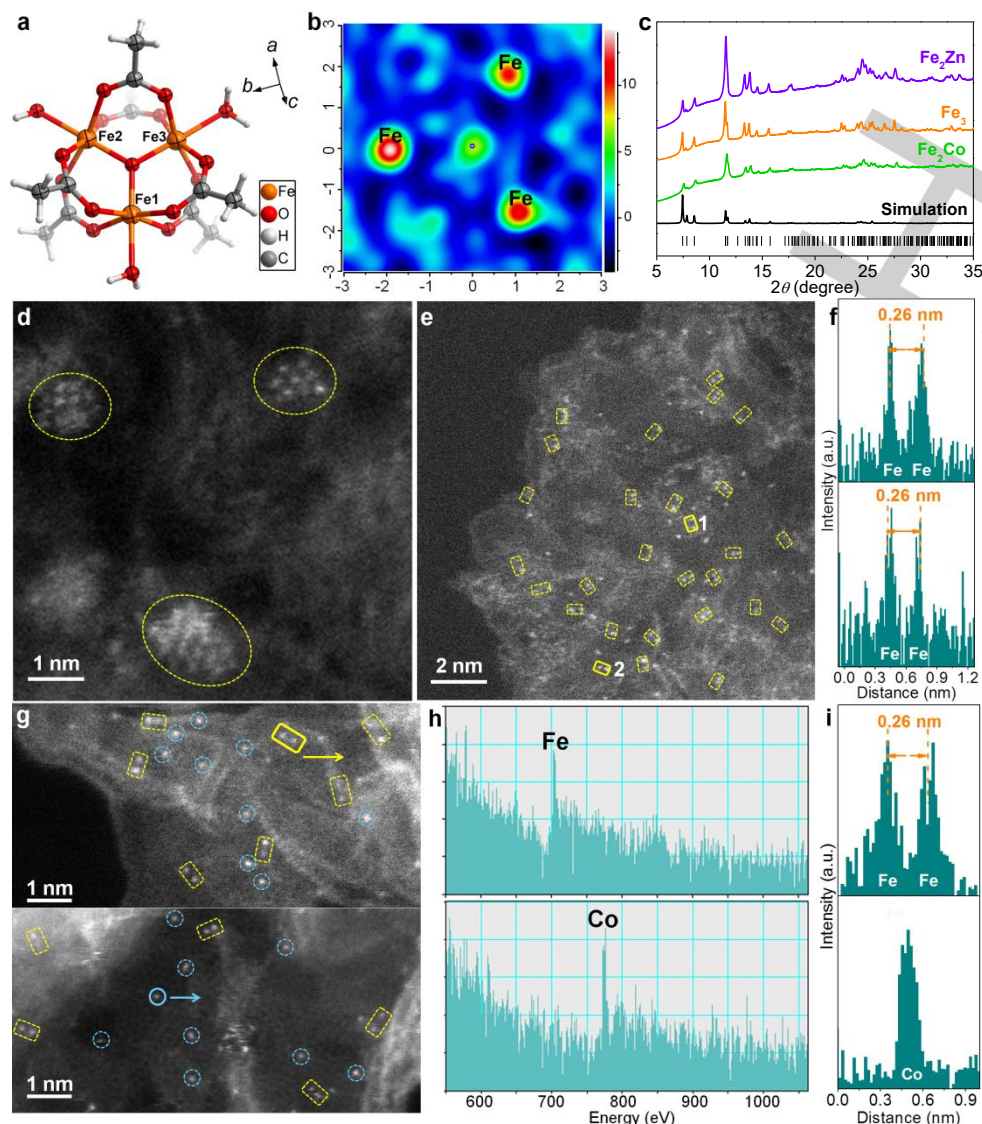


Figure 2. (a) Perspective view of the coordination environments around metal ions in Fe_3 . (b) Difference electron density maps for Fe_3 , showing the presence of trinuclear metal structure. (c) PXRD patterns. (d, e) HAADF-STEM images of Fe_3 -NPs/GNCL and Fe_2 -GNCL. (f) Intensity profiles (top and bottom) from the atomic sites 1 and 2 in g. (g) HAADF-STEM images of Fe_2/Co_1 -GNCL. The spots highlighted by dashed yellow boxes and blue circles indicate the possible dual Fe-Fe and single Co sites, respectively. (h) Single atom EELS spectroscopy (EELS) of Fe and Co, and i, intensity profiles highlighted in yellow and blue in (g) respectively. Notes for (g): white line edges at 708 eV for Fe-L_3 , 779 eV for Co-L_3 and 1020 eV for Zn-L_3 .

4.6 Å, which can be considered as the single Fe or Co atoms (Figure S45).

The huge differences prompt us to further investigate the real structures of these Fe/Co moieties stabilized in these materials. Considering a fact that TEM measurements hardly provide a complete determination for all the metal species within these materials, a more comprehensive inspection for the fine metal structures should draw much support from other statistical characterization methods, such as, XPS and XAFS spectra. Accordingly, XPS was then employed to analyze the chemical composition on the material surface. The high-resolution N 1s spectra of all the materials confirm the presences of pyridinic (398.1 eV) and graphitic (400.7 eV) species (Figures 3a and S46). Notably, differing from bare substrate GNCL, samples of Fe_2 -GNCL, Fe_2/Co_1 -GNCL and Fe_1/Co_1 -GNCL exhibit the metal-nitrogen (M-N) moieties at 399.3 eV,^[23a, 25] where the position is well consistent with that of N atoms (399.4 eV) of BPB^{2-} ligands bonded to Zn(II) ions in AIST-1. Obviously, these results strongly

suggest that Fe/Co atoms are coordinated with N sites on the GNCL.

Element-selective XAFS, including X-ray absorption near-edge spectroscopy (XANES) and extended X-ray absorption fine structure (EXAFS) spectroscopy, is a powerful tool to probe the chemical state and coordination environment of absorbing central atom with high sensitivity (Figures 3b-3g and S47-S49). Figure 3b shows the Fe *K*-edge XANES profiles for Fe_2/Co_1 -GNCL, Fe_2 -GNCL, and Fe_1/Co_1 -GNCL along with iron phthalocyanine (FePc) and Fe foil as their reference samples. Remarkably, different from that of Fe foil, Fe_2/Co_1 -GNCL presents an identical near-edge structure with that of Fe_2 -GNCL, which is similar to that of FePc, indicating that the average valence state of Fe should be close to +2 in Fe_2/Co_1 -GNCL and Fe_2 -GNCL. Nevertheless, the fingerprint peak (shown by FePc) ascribed to square-planar Fe-N_4 moiety with high D_{4h} symmetry is absent in both Fe_2/Co_1 -GNCL and Fe_2 -GNCL.^[25] This result

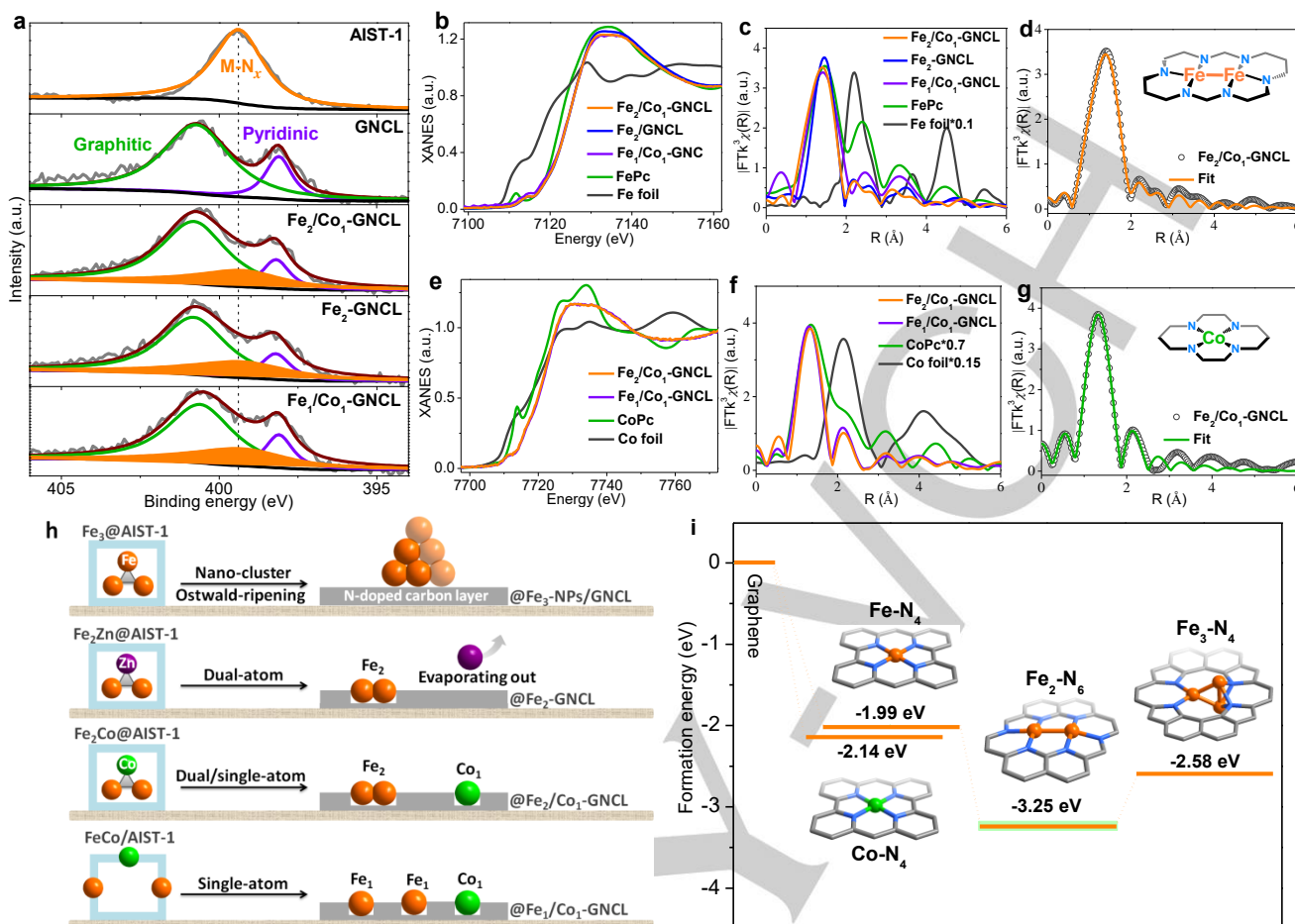


Figure 3. (a) High-resolution N 1s. (b) Fe *K*-edge XANES spectra. (c) FT k^3 -weighted (k)-function of the corresponding EXAFS spectra. (d) Fe *K*-edge EXAFS fitting curves of Fe_2/Co_1 -GNCL. Inset: Proposed architecture of the Fe-Fe cluster in Fe_2/Co_1 -GNCL. (e) Co *K*-edge XANES spectra. (f) FT k^3 -weighted (k)-function of the corresponding EXAFS spectra. (g) Co *K*-edge EXAFS fitting curves of Fe_2/Co_1 -GNCL. Inset: Proposed architecture of the single Co atom in Fe_2/Co_1 -GNCL. (h) The various thermal clustering fashions of iron atoms from different precursors based on AIST-1. (i) Formation energies of Fe/Co- N_4 , Fe_2 - N_6 and Fe_3 - N_4 moieties from graphene.

suggests that Fe species in these materials may exhibit a similar coordination configuration as Fe-N_4 with N atoms, but the D_{4h} symmetry should be distorted and reduced by other coordination bond, i.e. metal-metal.^[26] The coordination configurations were then determined with the FT (Fourier transformed) k^3 -weighted $\chi(k)$ -function of the corresponding EXAFS spectra in R space (Figures 3c and S47). The first strong FT profiles of Fe *K*-edge in Fe_2/Co_1 -GNCL and Fe_2 -GNCL resembled the reference samples of Fe_1/Co_1 -GNCL and FePc with a peak at ca. 1.40 Å (without phase shift correction), indicating the dominant Fe-N coordination.^{47,48} Interestingly, in both Fe_2/Co_1 -GNCL and Fe_2 -GNCL, the secondary peak was definitely observed at ca. 2.20 Å that can not be found in the Fe_1/Co_1 -GNCL and FePc, strongly demonstrating the existence of Fe-Fe coordination.^{45,46,49,50} To further elucidate the details of the structure, density functional theory (DFT) was employed to deduce the possible Fe-Fe structural configuration based on EXAFS experimental spectra and fitted FT curves (Figures 3d and S47). As a result, a calculated Fe_2 - N_6 architectural model matched excellently with experimental spectra. Compared with the Fe *K*-edge curves in Fe_2/Co_1 -GNCL and Fe_2 -GNCL, irrespective of the metal centers, the FT profiles of Co *K*-edge in Fe_2/Co_1 -GNCL and Fe_1/Co_1 -GNCL are almost identical (Figures 2e and S48), strongly indicating another coordination configuration, namely single-

atom Co- N_4 model obtained by EXAFS curve-fitting analyses similar with some recently reported single-atom catalysts (SACs).^[27]

Figure 3h provides a schematic illustration to systematically summarize and compare the aggregation behaviors of metal atoms within the above samples, coupled with the results of theoretical calculations (Figure 3i). The dominant presence of iron nanoclusters within Fe_3 -NPs/GNCL actually implies that the Fe_3 complex precursor may first thermally transform into an unstable iron trimer cluster, which should easily undergo a well-known Ostwald-ripening process to form the iron nanoclusters on the well-defined GNCL.^[8] This phenomenon inspires us to further study how to modulate this thermal aggregation behavior through the HMA strategy we developed. Specifically, when a thermally removable Zn atom replace the Fe(II) ion of the Fe_3 complex, merely dual iron atoms are expectedly observed in Fe_2 -GNCL, indicating the generated Zn metals can be evaporated out and Fe_2 - N_6 moiety should be a more stable metal species than the hypothetical iron trimer cluster, which is strongly supported by the theoretical calculation (Figure 3i). That is, the dual iron atoms can adopt an optimal coordination configuration (Fe_2 - N_6) with formation energy of -3.25 eV, which is less than those of Fe_3 - N_4 (-2.58 eV) and even single atom of Fe/Co- N_4 (-1.99/-2.14 eV). Furthermore, the above analyses are

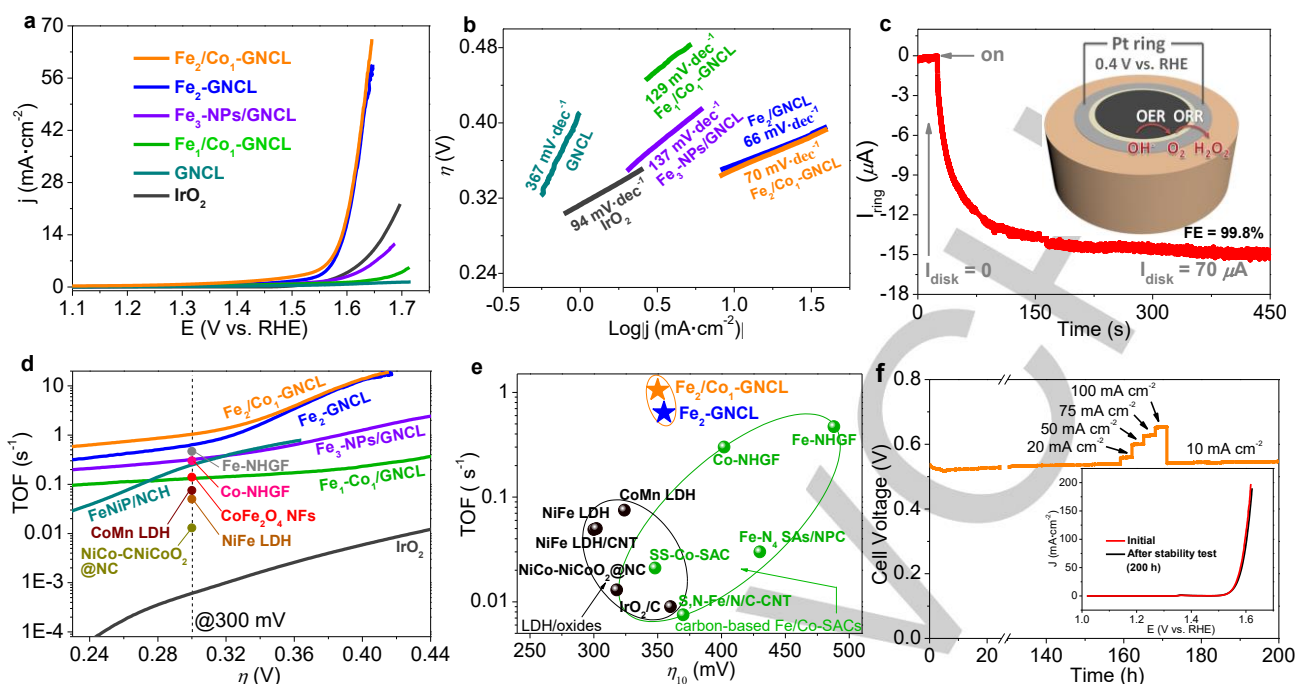


Figure 4. (a) OER polarization curves in 1 M KOH on glassy carbon electrode (GCE) with a scan rate of $10 \text{ mV}\cdot\text{s}^{-1}$. (b) The corresponding Tafel curves. (c) Faradaic efficiency (FE) testing of $\text{Fe}_2/\text{Co}_1\text{-GNCL}$ for OER using RRDE measurement (shown as an inset). (d) TOF values of the $\text{Fe}_2/\text{Co}_1\text{-GNCL}$ catalyst and other recently reported OER Fe/Co-based catalysts (Table S6). (e) TOF values of the $\text{Fe}_2/\text{Co}_1\text{-GNCL}$ catalyst with reported SACs (highlighted in violet circle) and Fe/Co-based LDH/oxides (highlighted in black circle). (f) Time-dependent potential curve for $\text{Fe}_2/\text{Co}_1\text{-GNCL}$ at a constant current density of $10 \text{ mA}\cdot\text{cm}^{-2}$. Insets: LSV curves before and after the stability test.

accordingly verified in the $\text{Fe}_2/\text{Co}_1\text{-GNCL}$ with concurrent formation of single Co atoms and dual iron atoms separately embedded in the GNCL. Obviously, the formation of stable iron-dimer cluster within $\text{Fe}_2\text{-GNCL}$ and $\text{Fe}_2/\text{Co}_1\text{-GNCL}$ successfully realizes the inhibition of iron atoms aggregating toward nanoclusters during their synthesis, which hardly occurs in $\text{Fe}_3\text{-NPs/GNCL}$ owing to the unsuitable number of metal atoms contained in the Fe_3 complex precursor. With respect to the $\text{Fe}_1/\text{Co}_1\text{-GNCL}$, only uniformly dispersed single Fe and Co atoms are found due to the absence of HMA strategy. These rare achievements should be attributed to the successful application of our precise synthesis strategy, and are believed to significantly facilitate elucidating the forming process and guiding the structural design of future supported USMCs at atomic scale.

Experimental Evaluation on Oxygen Evolution Activities.

Engineering coordination environments of the supported metal sites are crucial for modifying their electronic and geometric properties, thus affecting electrocatalytic activity and stability.^[28] Among these diverse metal species within the carbon layers, the unique and stable dual iron atoms architecture actually provides a great opportunity to investigate their cooperative capacities that govern reactant molecules into favorable conformations for lowering the transition state energies of given chemical transformations,^[25-26, 29] e.g., oxygen evolution reaction (OER) (Figure S50). We therefore proceeded to verify the cooperative OER catalytic activity of dual iron atoms by the electrochemical measurements. Considering the identical morphology of these materials, we first confirmed that they have similar electrochemical surface areas (ECSAs) through measuring their double-layer capacitances (C_{dl}) (Figures S51 and S52), effectively excluding other unknown contributors for the

electrocatalytic activity except for the different metal sites. Afterwards, as shown in Figure 4a, $\text{Fe}_2\text{-GNCL}$ and $\text{Fe}_2/\text{Co}_1\text{-GNCL}$ present identical OER polarization curves with similar overpotential at $10 \text{ mA}\cdot\text{cm}^{-2}$ ($\eta_{10} = 355$ and 350 mV , respectively), significantly outperforming those of $\text{Fe}_3\text{-NPs/GNCL}$ (447 mV), $\text{Fe}_1/\text{Co}_1\text{-GNCL}$ ($> 480 \text{ mV}$), IrO_2 (420 mV) and most of reported MOF-derived atomically dispersed metal electrocatalysts (Table S6). This experimentally observed trend clearly confirmed that the Fe-Fe sites should possess the main catalytic activities toward oxygen evolution among the diverse metal sites. Additionally, the Tafel slopes of $\text{Fe}_2\text{-GNCL}$ ($66 \text{ mV}\cdot\text{dec}^{-1}$) and $\text{Fe}_2/\text{Co}_1\text{-GNCL}$ ($70 \text{ mV}\cdot\text{dec}^{-1}$) are much smaller than those of $\text{Fe}_3\text{-NPs/GNCL}$ ($137 \text{ mV}\cdot\text{dec}^{-1}$), $\text{Fe}_1/\text{Co}_1\text{-GNCL}$ ($129 \text{ mV}\cdot\text{dec}^{-1}$) and IrO_2 ($94 \text{ mV}\cdot\text{dec}^{-1}$), also demonstrating the key roles of dual-atom iron catalyst in promoting the OER reaction kinetics (Figure 4b).

To guarantee that the observed oxidation current really comes from the oxygen evolution, a rotating ring disk electrode (RRDE) method was employed to confirm no obvious by-product peroxide and a favorable four-electron process ($4\text{OH}^- \rightarrow \text{O}_2 + 2\text{H}_2\text{O} + 4\text{e}^-$) as well as a high Faradaic efficiency (99.8%) during electrocatalysis (Figures S53 and 4c). These results indicate that the observed oxidation current of $\text{Fe}_2/\text{Co}_1\text{-GNCL}$ originates exclusively from the oxygen evolution (Figures 4c). With regard to turnover frequency (TOF) compared with other related materials, $\text{Fe}_2\text{-GNCL}$ and $\text{Fe}_2/\text{Co}_1\text{-GNCL}$ are among the best OER electrocatalysts with the highest utilization efficiency of active metal atoms (Figure 4d). For instance, at 300 mV overpotential, the TOF of $\text{Fe}_2/\text{Co}_1\text{-GNCL}$ (1.05 s^{-1}) is better than those of most reported carbon-supported SACs, and even two orders of magnitude higher than those of Fe/Co-based layered double hydroxides (LDHs) (Figure 4e and Table S6), strongly

implying an excellent cooperativity in improving electrocatalytic kinetics at the dual-atom iron catalyst for oxygen evolution.

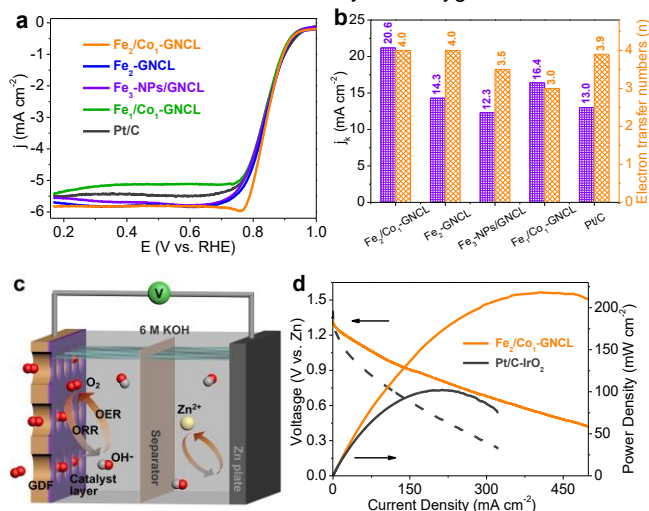


Figure 5. (a) ORR polarization of Fe₂/Co₁-GNCL and control samples in O₂-saturated 0.1 M KOH solution with RDE rotation rate of 1600 rpm. (b) Specific activity at 0.812 V and electron transfer numbers (*n*) for ORR activities. (c) Representation of Zn-air battery (GDF: gas diffusion film). (d) Battery voltage and power density of Zn-air batteries assembled by Fe₂/Co₁-GNCL and the state-of-the-art catalyst (Pt/C-IrO₂), respectively.

Additionally, the reaction durability was well verified through carrying out the catalytic reaction under different current densities (10 ~ 100 mA cm⁻²) for over 200 h (Figure 4f), strongly proving the excellent robustness of Fe-Fe site in the coordinating matrix during the electrocatalytic OER operation condition. The inherent excellent OER activity greatly prompted us to study its catalysis for the oxygen reduction reaction (ORR), and thus possibly use it to fabricate a rechargeable Zn-air battery to evaluate its potential for practical applications.^[30] Notably, both the dual-atom iron catalyst and single Co site have been considered as efficient electrocatalytic centers for ORR in terms of theoretical and experimental evaluation.^[18b, 31] Expectedly, as shown in the polarization curves for ORR (Figures 5a, 5b and S54-S59), Fe₂/Co₁-GNCL presented a larger kinetic current density (20.6 mA cm⁻²) and higher electron transfer number (4.0) than those of Fe₂-GNCL, Fe₃-NPs/GNCL, Fe₁/Co₁-GNCL and Pt/C, indicating the more favorable electrocatalytic kinetics for oxygen reduction of Fe₂/Co₁-GNCL (Figures S60-S63 and Table S7). Given the outstanding bifunctional electrochemical activities of Fe₂/Co₁-GNCL, a two-electrode rechargeable zinc-air battery was assembled to evaluate its performances for practical applications (Figures 5c, 5d and S64-66). As a result, this battery can work stably with a superior peak power density (218 mW cm⁻²) compared with that (101 mW cm⁻²) of the state-of-the-art catalyst (Pt/C-IrO₂) (Table S8), which should be possibly ascribed to the high catalytic activity of these robust atomically dispersed metal-metal sites, and presents a huge potential in future practical applications.

Conclusion

In summary, we designed and constructed a unique MOF structurally featuring abundant ordered aromatic ring arrays, which is capable of upgrading as a well-defined nitrogen-doped carbon layer. Significantly, based on this platform material, a

heteroatom modulator approach has been developed to reveal a definitive correlation of supported metal cluster fashions with the species and numbers of metal atoms. By virtue of the powerful XAFS analyses and direct TEM imaging, together with theoretical calculations, we clearly identified that the supported dual-atom iron is stabilized in an optimal metal-nitrogen moiety within the carbon layer, which can experimentally behave as cooperative metal-metal sites for efficient oxygen evolution catalysis. The concepts, approaches and results presented by this work would serve as valuable guidances for the future design of highly active USMCs for catalysis.

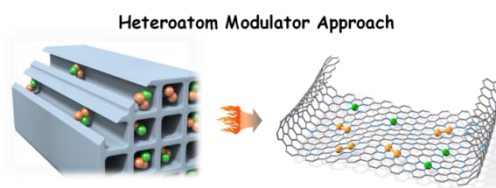
Acknowledgements

This article is dedicated to the people fighting against the Coronavirus disease (COVID-19) pandemic. We acknowledge financial support from AIST. J. H. and K.S. acknowledge the support from JST Research Acceleration Programme and JSPS-KAKENHI (JP16H06333 and JP17H04797). We thank Ms. Nanae Shimanaka, Dr. Mingshui Yao and Dr. Yifan Gu of KUIAS-iCeMS, Kyoto University for the single crystal X-ray diffraction measurements and Aichi Synchrotron Radiation Center for measurement supports of X-ray absorption fine structure (XAFS) analyses (2019ND601, 2019ND602).

Keywords: Metal–Organic Framework, Metal Nanocluster, Single Atom Catalyst, Oxygen Evolution Reaction, Zn-Air Battery.

- [1] a) X. Cui, W. Li, P. Ryabchuk, K. Junge, M. Beller, *Nat. Catal.* **2018**, *1*, 385-397; b) E. C. Tyo, S. Vajda, *Nat. Nanotechnol.* **2015**, *10*, 577-588; c) Y. Lu, W. Chen, *Chem. Soc. Rev.* **2012**, *41*, 3594-3623; d) L. Zhang, M. Zhou, A. Wang, T. Zhang, *Chem. Rev.* **2020**, *120*, 683-733; e) Z. Li, S. Ji, Y. Liu, X. Cao, S. Tian, Y. Chen, Z. Niu, Y. Li, *Chem. Rev.* **2020**, *120*, 623-682.
- [2] R.-W. Huang, Y.-S. Wei, X.-Y. Dong, X.-H. Wu, C.-X. Du, S.-Q. Zang, T. C. W. Mak, *Nat. Chem.* **2017**, *9*, 689-697.
- [3] a) R. Blum, J. E. S. van der Hoeven, J. Hulva, J. Pavelec, O. Gamba, P. E. de Jongh, M. Schmid, P. Blaha, U. Diebold, G. S. Parkinson, *Proc. Natl. Acad. Sci. U.S.A.* **2016**, *113*, 8921-8926; b) B. Weng, K.-Q. Lu, Z. Tang, H. M. Chen, Y.-J. Xu, *Nat. Commun.* **2018**, *9*, 1543.
- [4] F. R. Fortea-Pérez, M. Mon, J. Ferrando-Soria, M. Boronat, A. Leyva-Pérez, A. Corma, J. M. Herrera, D. Osadchii, J. Gascon, D. Armentano, E. Pardo, *Nat. Mater.* **2017**, *16*, 760-766.
- [5] a) X. Kang, M. Zhu, *Chem. Soc. Rev.* **2019**, *48*, 2422-2457; b) Y. Du, H. Sheng, D. Astruc, M. Zhu, *Chem. Rev.* **2020**, *120*, 526-622.
- [6] Y. Song, E. Ozdemir, S. Ramesh, A. Adishev, S. Subramanian, A. Harale, M. Albuali, B. A. Fadhel, A. Jamal, D. Moon, S. H. Choi, C. T. Yavuz, *Science* **2020**, *367*, 777-781.
- [7] D.-e. Jiang, S. H. Overbury, S. Dai, *J. Phys. Chem. C* **2012**, *116*, 21880-21885.
- [8] a) J. B. Hannon, S. Kodambaka, F. M. Ross, R. M. Tromp, *Nature* **2006**, *440*, 69-71; b) C. T. Campbell, S. C. Parker, D. E. Starr, *Science* **2002**, *298*, 811-814; c) J. Yang, Z. Qiu, C. Zhao, W. Wei, W. Chen, Z. Li, Y. Qu, J. Dong, J. Luo, Z. Li, Y. Wu, *Angew. Chem.* **2018**, *130*, 14291-14296; *Angew. Chem., Int. Ed.* **2018**, *57*, 14095-14100.
- [9] a) K. Kwak, W. Choi, Q. Tang, M. Kim, Y. Lee, D.-e. Jiang, D. Lee, *Nat. Commun.* **2017**, *8*, 14723; b) H. Häkkinen, *Nat. Chem.* **2012**, *4*, 443-455.
- [10] a) H. Li, M. Eddaoudi, M. O'Keeffe, O. M. Yaghi, *Nature* **1999**, *402*, 276-279; b) K. Shen, L. Zhang, X. Chen, L. Liu, D. Zhang, Y. Han, J. Chen, J. Long, R. Luque, Y. Li, B. Chen, *Science* **2018**, *359*, 206-210; c) M. Zhao, Y. Huang, Y. Peng, Z. Huang, Q. Ma, H. Zhang, *Chem. Soc. Rev.* **2018**, *47*, 6267-6295; d) S.-H. Lo, L. Feng, K. Tan, Z. Huang, S. Yuan, K.-Y. Wang, B.-H. Li,

- W.-L. Liu, G. S. Day, S. Tao, C.-C. Yang, T.-T. Luo, C.-H. Lin, S.-L. Wang, S. J. L. Billinge, K.-L. Lu, Y. J. Chabal, X. Zou, H.-C. Zhou, *Nat. Chem.* **2020**, *12*, 90-97; e) G. Férey, C. Mellot-Draznieks, C. Serre, F. Millange, J. Dutour, S. Surblé, I. Margiolaki, *Science* **2005**, *309*, 2040-2042; f) S. M. J. Rogge, A. Bavykina, J. Hajek, H. Garcia, A. I. Olivos-Suarez, A. Sepúlveda-Escribano, A. Vimont, G. Clet, P. Bazin, F. Kapteijn, M. Daturi, E. V. Ramos-Fernandez, F. X. Llabrés i Xamena, V. Van Speybroeck, J. Gascon, *Chem. Soc. Rev.* **2017**, *46*, 3134-3184; g) H. Zhong, M. Ghorbani-Asl, K. H. Ly, J. Zhang, J. Ge, M. Wang, Z. Liao, D. Makarov, E. Zschech, E. Brunner, I. M. Weidinger, J. Zhang, A. V. Krashennikov, S. Kaskel, R. Dong, X. Feng, *Nat. Commun.* **2020**, *11*, 1409.
- [11] O. M. Yaghi, M. O'Keeffe, N. W. Ockwig, H. K. Chae, M. Eddaoudi, J. Kim, *Nature* **2003**, *423*, 705-714.
- [12] a) B. Liu, H. Shioyama, T. Akita, Q. Xu, *J. Am. Chem. Soc.* **2008**, *130*, 5390-5391; b) P. Pachfule, D. Shinde, M. Majumder, Q. Xu, *Nat. Chem.* **2016**, *8*, 718-724; c) S. Dang, Q.-L. Zhu, Q. Xu, *Nat. Rev. Mater.* **2017**, *3*, 17075; d) R. V. Jagadeesh, K. Murugesan, A. S. Alshammari, H. Neumann, M.-M. Pohl, J. Radnik, M. Beller, *Science* **2017**, *358*, 326-332; e) Y.-S. Wei, M. Zhang, M. Kitta, Z. Liu, S. Horike, Q. Xu, *J. Am. Chem. Soc.* **2019**, *141*, 7906-7916; f) W. Xia, R. Zou, L. An, D. Xia, S. Guo, *Energy Environ. Sci.* **2015**, *8*, 568-576.
- [13] Y.-S. Wei, M. Zhang, R. Zou, Q. Xu, *Chem. Rev.* **2020**, DOI: 10.1021/acs.chemrev.9b00757.
- [14] Q. Wang, D. Astruc, *Chem. Rev.* **2020**, *120*, 1438-1511.
- [15] a) Z. Liang, R. Zhao, T. Qiu, R. Zou, Q. Xu, *EnergyChem* **2019**, *1*, 100001; b) H. Jin, C. Guo, X. Liu, J. Liu, A. Vasileff, Y. Jiao, Y. Zheng, S.-Z. Qiao, *Chem. Rev.* **2018**, *118*, 6337-6408.
- [16] L. Chong, J. Wen, J. Kubal, F. G. Sen, J. Zou, J. Greeley, M. Chan, H. Barkholtz, W. Ding, D.-J. Liu, *Science* **2018**, *362*, 1276-1281.
- [17] a) Y.-C. Lin, P.-Y. Teng, P.-W. Chiu, K. Suenaga, *Phys. Rev. Lett.* **2015**, *115*, 206803; b) H. Fei, J. Dong, Y. Feng, C. S. Allen, C. Wan, B. Voloskiy, M. Li, Z. Zhao, Y. Wang, H. Sun, P. An, W. Chen, Z. Guo, C. Lee, D. Chen, I. Shakir, M. Liu, T. Hu, Y. Li, A. I. Kirkland, X. Duan, Y. Huang, *Nat. Catal.* **2018**, *1*, 63-72.
- [18] a) S. Ji, Y. Chen, Q. Fu, Y. Chen, J. Dong, W. Chen, Z. Li, Y. Wang, L. Gu, W. He, C. Chen, Q. Peng, Y. Huang, X. Duan, D. Wang, C. Draxl, Y. Li, *J. Am. Chem. Soc.* **2017**, *139*, 9795-9798; b) W. Ye, S. Chen, Y. Lin, L. Yang, S. Chen, X. Zheng, Z. Qi, C. Wang, R. Long, M. Chen, J. Zhu, P. Gao, L. Song, J. Jiang, Y. Xiong, *Chem* **2019**, *5*, 2865-2878.
- [19] N. Masciocchi, G. A. Ardizzoia, A. Maspero, G. LaMonica, A. Sironi, *Inorg. Chem.* **1999**, *38*, 3657-3664.
- [20] M. O'Keeffe, M. A. Peskov, S. J. Ramsden, O. M. Yaghi, *Acc. Chem. Res.* **2008**, *41*, 1782-1789.
- [21] W. Zhang, X. Jiang, X. Wang, Y. V. Kaneti, Y. Chen, J. Liu, J.-S. Jiang, Y. Yamauchi, M. Hu, *Angew. Chem.* **2017**, *129*, 8555-8560; *Angew. Chem., Int. Ed.* **2017**, *56*, 8435-8440.
- [22] L. El Hanache, B. Lebeau, H. Nouali, J. Toufaily, T. Hamieh, T. J. Daou, *J. Hazard. Mater.* **2019**, *364*, 206-217.
- [23] a) J. Li, M. Chen, D. A. Cullen, S. Hwang, M. Wang, B. Li, K. Liu, S. Karakalos, M. Lucero, H. Zhang, C. Lei, H. Xu, G. E. Sterbinsky, Z. Feng, D. Su, K. L. More, G. Wang, Z. Wang, G. Wu, *Nat. Catal.* **2018**, *1*, 935-945; b) W. Cai, T. Lee, M. Lee, W. Cho, D.-Y. Han, N. Choi, A. C. K. Yip, J. Choi, *J. Am. Chem. Soc.* **2014**, *136*, 7961-7971.
- [24] a) A. Aijaz, A. Karkamkar, Y. J. Choi, N. Tsumori, E. Rönnebro, T. Autrey, H. Shioyama, Q. Xu, *J. Am. Chem. Soc.* **2012**, *134*, 13926-13929; b) Q.-L. Zhu, J. Li, Q. Xu, *J. Am. Chem. Soc.* **2013**, *135*, 10210-10213.
- [25] W. Ren, X. Tan, W. Yang, C. Jia, S. Xu, K. Wang, S. C. Smith, C. Zhao, *Angew. Chem.* **2019**, *131*, 7046-7050; *Angew. Chem., Int. Ed.* **2019**, *58*, 6972-6976.
- [26] a) J. Wang, Z. Huang, W. Liu, C. Chang, H. Tang, Z. Li, W. Chen, C. Jia, T. Yao, S. Wei, Y. Wu, Y. Li, *J. Am. Chem. Soc.* **2017**, *139*, 17281-17284; b) S. Tian, Q. Fu, W. Chen, Q. Feng, Z. Chen, J. Zhang, W.-C. Cheong, R. Yu, L. Gu, J. Dong, J. Luo, C. Chen, Q. Peng, C. Draxl, D. Wang, Y. Li, *Nat. Commun.* **2018**, *9*, 2353.
- [27] a) R. Zhao, Z. Liang, S. Gao, C. Yang, B. Zhu, J. Zhao, C. Qu, R. Zou, Q. Xu, *Angew. Chem.* **2019**, *131*, 1997-2001; *Angew. Chem., Int. Ed.* **2019**, *58*, 1975-1979; b) L. Jiao, G. Wan, R. Zhang, H. Zhou, S.-H. Yu, H.-L. Jiang, *Angew. Chem.* **2018**, *130*, 8661-8665; *Angew. Chem., Int. Ed.* **2018**, *57*, 8525-8529; c) F. Pan, H. Zhang, K. Liu, D. Cullen, K. More, M. Wang, Z. Feng, G. Wang, G. Wu, Y. Li, *ACS Catal.* **2018**, *8*, 3116-3122; d) M. Xiao, L. Gao, Y. Wang, X. Wang, J. Zhu, Z. Jin, C. Liu, H. Chen, G. Li, J. Ge, Q. He, Z. Wu, Z. Chen, W. Xing, *J. Am. Chem. Soc.* **2019**, *141*, 19800-19806.
- [28] a) Y. Zhu, J. Sokolowski, X. Song, Y. He, Y. Mei, G. Wu, *Adv. Energy Mater.* **2020**, *10*, 1902844; b) Q. Shi, S. Hwang, H. Yang, F. Ismail, D. Su, D. Higgins, G. Wu, *Mater. Today* **2020**, DOI: 10.1016/j.mattod.2020.02.019.
- [29] a) S. Sarkar, A. Biswas, T. Purkait, M. Das, N. Kamboj, R. S. Dey, *Inorg. Chem.* **2020**, *59*, 5194-5205; b) J. Wang, R. You, C. Zhao, W. Zhang, W. Liu, X.-P. Fu, Y. Li, F. Zhou, X. Zheng, Q. Xu, T. Yao, C.-J. Jia, Y.-G. Wang, W. Huang, Y. Wu, *ACS Catal.* **2020**, *10*, 2754-2761.
- [30] H.-F. Wang, C. Tang, B. Wang, B.-Q. Li, Q. Zhang, *Adv. Mater.* **2017**, *29*, 1702327.
- [31] P. Yin, T. Yao, Y. Wu, L. Zheng, Y. Lin, W. Liu, H. Ju, J. Zhu, X. Hong, Z. Deng, G. Zhou, S. Wei, Y. Li, *Angew. Chem.* **2016**, *128*, 10958-10963; *Angew. Chem., Int. Ed.* **2016**, *55*, 10800-10805.

Entry for the Table of Contents

Derived from a trinuclear $\text{Fe}^{\text{III}}_2\text{Fe}^{\text{II}}$ complex encapsulated within the channels of a unique MOF, the generated iron nanoclusters stabilized on the carbon layer can be achieved. To realize the inhibition of iron atoms aggregating toward nanoclusters, we developed a “Heteroatom Modulator Approach”, that is, atomic replacements of the Fe^{II} by $\text{Zn}^{\text{II}}/\text{Co}^{\text{II}}$ to successfully synthesize a stable iron dimer in an optimal metal-nitrogen moiety, which has been experimentally demonstrated for efficient oxygen evolution catalysis.